
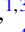









Using optical spectroscopy to probe the impact of atomic disorder on the Heusler alloy Co_2MnGa Ben Mallett ^{1,3}, Yao Zhang ^{1,3}, Catherine Pot ^{2,3}, Kiri Van Koughnet ^{1,2}, Blake Stanley,¹ Robert G. Buckley ^{1,3}, Annette Koo ⁴, Yuefeng Yin ^{5,6}, Nikhil V. Medhekar ^{5,6} and Simon Granville ^{1,3}¹Robinson Research Institute, Victoria University of Wellington, P.O. Box 33436, Petone 5046, New Zealand²School of Chemical and Physical Sciences, Victoria University of Wellington, P.O. Box 600, Wellington 6140, New Zealand³MacDiarmid Institute for Advanced Materials and Nanotechnology, P.O. Box 600, Wellington 6140, New Zealand⁴Measurement Standards Laboratory of New Zealand, Callaghan Innovation, P.O. Box 31310, Lower Hutt 5040, New Zealand⁵Department of Materials Science and Engineering, Monash University, Clayton, Victoria 3800, Australia⁶ARC Centre of Excellence in Future Low-Energy Electronics Technologies, Clayton, Victoria 3800, Australia

(Received 19 December 2022; accepted 28 June 2023; published 14 September 2023)

The exceptional electronic and spintronic properties of magnetic Heusler alloys, which include half-metals and Weyl semimetals, are strongly sensitive to deviations from the ideal atomic structure. To ensure that these materials have been produced with the desired properties, it is necessary to determine both the structural ordering and the electronic structure, which can be challenging. Here, we present the results of a far-infrared-to-visible optical spectroscopy study of films of room-temperature ferromagnetic Weyl semimetal Co_2MnGa . Combined with a determination of the level of ordering from x-ray diffraction, we have investigated near Fermi energy valence and conduction band intra- and interband transitions and their dependence on the atomic order. Motivated by band structure calculations, we have modeled our optical spectra with two Drude terms and two Lorentz oscillators, where the latter are assigned to interband transitions. The scattering rate of the itinerant carriers, determined from the width of the Drude term, increases threefold with increasing disorder, while the carrier density to effective mass ratio is unchanged. Based on our band structure and the joint density of states calculations, we have assigned the oscillator that dominates the interband spectral region near 1 eV to transitions across the minority spin gap along the Γ - X direction. It is found that the energy of this transition is strongly sensitive to the degree of order and decreases rapidly with increasing disorder as states fill a decreasing minority spin gap. Our results demonstrate optical spectroscopy is a sensitive way to fingerprint structural order in the technologically relevant near Fermi level electronic states in Heusler alloys.

DOI: [10.1103/PhysRevMaterials.7.094203](https://doi.org/10.1103/PhysRevMaterials.7.094203)

I. INTRODUCTION

Full Heusler alloys with the general formula, X_2YZ , where X and Y are transition metals and Z is a main group element, exhibit a wide range of electronic and magnetic properties. Depending on their structure and composition they can be insulating through to superconducting [1] or with topologically nontrivial states [2–4]. Of special interest for applications are compositions that form half-metals, where below a ferromagnetic Curie temperature T_c , the electronic states are spin polarized with the majority spin bands crossing the Fermi level while the minority spin bands are gapped across the Fermi level [5–8]. Numerous examples are compounds with $X = \text{Co}$ and $Y = \text{Mn}$, which have been predicted to be half-metals with a T_c above room temperature [9]. Of special interest is Co_2MnGa , which is a topological Weyl semimetal with a T_c of 694 K [10,11] displaying at room temperature a large intrinsic anomalous Hall effect (AHE) [8,12], anomalous Nernst effect (ANE) [13,14], and spin Hall effect [15] that arise from the presence of Weyl fermions which drive a large Berry curvature near the Fermi energy [8,16]. It has been shown, however, that the electronic band structure, and thus the Berry curvature, is sensitive to changes in the film's atomic order [17,18] and thickness [19]. Being able to describe the relationships between crystal structure, atomic ordering, and

the electronic properties of the Heusler alloys near the Fermi energy is critical for a full understanding and thus for their application.

Fully ordered Heusler alloys crystallize in the $L2_1$ structure, while random occupancy of the Y and Z sites is described as having a $B2$ structure, and complete disorder across all, X , Y , and Z sites as having an $A2$ structure [20]. While methods of estimating the degree of atomic order using x-ray diffraction (XRD) have been developed [21–23] it is in general very challenging, requiring advanced synchrotron, neutron diffraction, or high-resolution electron microscopy studies [24,25]. Nonetheless, several authors have correlated changes in the degree of atomic order to the electronic properties of some Heusler alloys [6,16,18,20,26].

The near Fermi energy electronic structure of the Co_2MnZ compounds is largely determined by the presence of Co-Co-Mn d - d hybridized bands [5,11,8]. When the Z atom is Si, Ge, or Sn (IVB element) the minority gap is large, and the Fermi energy lies within it, forming a half-metal. Where the Z atom is Al or Ga (IIIB element) the gap is smaller and, in the case where $Z = \text{Ga}$ the Fermi level lies at the bottom of the minority spin gap in a region of a small but finite density of states [11,27,28]. Recently, attention has been drawn to the role that atomic disorder plays in the Co_2MnZ compounds,

and notably the increase in electron states in the minority spin gap with increasing atomic disorder which destroys their half-metallicity [6,18,26].

For studying electronic states, one widely accessible experimental tool is optical spectroscopy, a technique that directly probes the bulk properties, the valence and conduction states near the Fermi level, and, notably, changes in the intra- and interband electronic behavior. However, only a few authors have published the results of optical studies on full-Heusler compositions including bulk [29–31] and films [32–34] and on half-Heusler compositions [35]. Rai and co-workers [36] have undertaken a computational study of the optical response. Here we present the results of an optical spectroscopic study of a series of Co_2MnGa films with different degrees of atomic order as determined by XRD. We have measured the energy dependent reflectivity and transmission from which we determine the energy dependent conductivity between 0.01 and 6 eV, identifying the behavior of both the itinerant carriers and interband transitions, with reference to direct current (DC) electrical transport measurements and calculations of the joint density of electronic states.

II. EXPERIMENTAL METHODS

Thin films of Co_2MnGa were deposited by DC magnetron sputtering using a Kurt J. Lesker CMS-18 system. The films were sputtered onto 10×10 mm double-side polished MgO (001) substrates from a composite target of $\text{Co}:\text{Mn}:\text{Ga}$ with a relative atomic composition of 50:25:25. The MgO (001) substrates were held in vacuum for 1 h at 400°C before deposition. All films were then grown at 400°C followed by *in situ* annealing in vacuum for times ranging from 0 (unannealed) to 60 min and at several temperatures between 400°C and 550°C . Film thicknesses were kept at 100 nm although one 200 nm film was deposited for optical measurements. Using the energy dispersive x-ray analysis (EDAX) capability of a FEI Quanta scanning electron microscope (SEM) the film compositions were determined to be close to stoichiometric Co_2MnGa composition, at $\text{Co}_{1.96}\text{Mn}_{0.96}\text{Ga}_{1.08}$. The compositional analysis calculation employed CALCZAF [37] and NIST DTSA-II [38] software and EDAX measurements from elemental standards. XRD spectra were collected using two instruments, a Bruker D8 Advance system and a Rigaku SmartLab, both using $\text{Co K}\alpha$ x-ray radiation at a wavelength of 1.7889 \AA . The experimental XRD spectra were compared to the theoretical Co_2MnGa XRD pattern calculated using the software VESTA [39]. The temperature-dependent resistivity and the anomalous Hall angle between 2 and 300 K were measured using a Quantum Design physical property measurement system (PPMS).

The reflectivity and transmission spectra were measured at room temperature employing a Bruker Vertex 80v interferometer from 10 meV to 3 eV [34]. For some samples we extended the spectral range to 6 eV by using a conventional grating monochromator. The reflectivity and transmission are measured relative to the incident beam. In the case of the reflectivity the incident intensity was measured using an evaporated Al film and corrected employing literature values for the aluminum reflectivity [40]. In the case of transmission, the incident light is measured through an open aperture, so

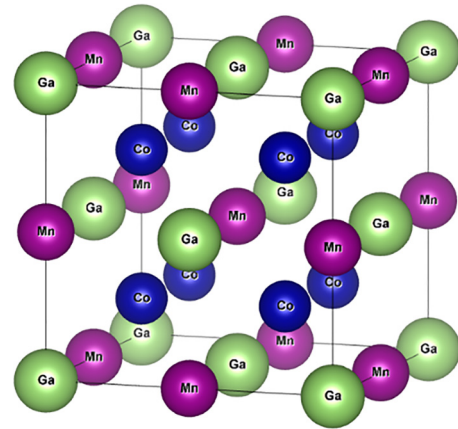


FIG. 1. A diagram illustrating the atomic positions of Co_2MnGa in the ideal $L2_1$ crystal structure. This picture was generated using the crystallographic simulation software VESTA [39].

no correction is required. We report room-temperature reflectivity and transmission measurements. The uncertainty in the magnitude of these quantities is $\pm 2\%$. The error in the magnitude was estimated from the reproducibility of the spectra and the mismatch in the magnitude of spectra collected across different spectral ranges.

As described elsewhere [19] we used density functional theory (DFT), within the generalized gradient approximation (GGA) [41], as implemented in the Vienna *ab initio* simulation package (VASP) [42], to calculate the electronic structure of Co_2MnGa .

III. FILM GROWTH AND CHARACTERIZATION

As illustrated in Fig. 1, fully ordered Co_2MnGa consists of four face-centered cubic sublattices, two of Co and one each of Mn and Ga, while crystallizing in the $L2_1$ crystal structure with space group $225 (Fm\bar{3}m)$. As illustrated in the XRD spectra of Fig. 2, the (002) and (004) lines were observed in all our films indicating (001) orientated growth, epitaxial with the MgO substrate. Furthermore, the presence of the (002) line indicates the $B2$ structure is present in all films. An optimized

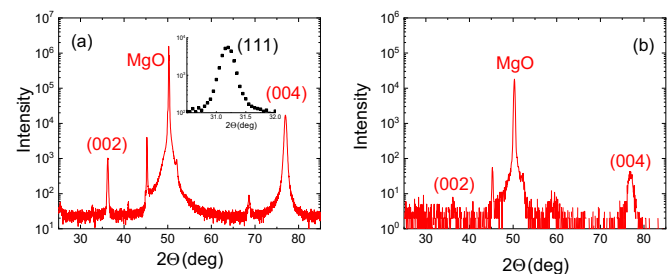


FIG. 2. (a) Out-of-plane θ - 2θ x-ray diffractograms for a Co_2MnGa film for which the (111)/(004) ratio is a maximum of 0.144. This pattern was collected on the Bruker D8 Advance system. The black inset is the (111) superlattice peak measured at an out-of-plane tilt of 53.92° . (b) Out-of-plane θ - 2θ x-ray diffractogram for a Co_2MnGa film for which the (111)/(004) ratio is zero; i.e., there is no observable (111) reflection. This pattern was collected on the Rigaku SmartLab.

TABLE I. A summary of the numbered films used in the optical study listing, respectively, their annealing conditions, predeposition pressure, (111)/(004) intensity ratio (proxy for L_{21} ordering), lattice parameter, 300 K DC conductivity, and thickness. We note that the uncertainty in the lattice parameter for film 5 is larger at ± 0.001 nm due to the very low scattering intensity of the (004) line in this film relative to that observed in other films.

Film	Annealing temperature (°C)/time (mins)	Predeposition pressure (10^{-7} mbar)	(111)/(004) Intensity ratio	Lattice parameter ± 0.001 (nm)	300 K DC conductivity (W cm^{-1})	Film thickness (nm)
1	550/60	1.5	0.144	0.5750	8130	200
2	400/20	1.5	0.139	0.5752	11 000	100
3	550/60	1.5	0.065	0.5746	8621	100
4	550/60	30	0.013	0.5735	4310	100
5	550/60	15	0.000	0.576	3984	100

deposition process was developed, guided by the temperature dependent resistivity, the anomalous Hall angle (AHA) [19], and notably the use of the XRD reflection intensities. The optimization process involved producing films with the highest ratio of the intensities of the superlattice (111) reflection to the fundamental (004) reflection, which we use as a proxy for the L_{21} structure [18]. By applying an out-of-plane tilt to the film of 53.92° during XRD measurements, the (111) plane can be accessed. We have used a proxy for the L_{21} order parameter as its calculation is not straightforward using conventional laboratory-based XRD equipment [20]. To achieve a reliable value for L_{21} the integrated intensity over a full ϕ scan is measured followed by the application of various corrections [25]. In the case of Co-containing Heusler alloy thin films it is also likely that two different wavelengths will be required due to the very similar atomic scattering factors of Co and Mn [25,43]. For these reasons values reported for L_{21} or $B2$ order are generally not readily comparable. As shown in Table I, our films showed a range of values for the (111)/(004) ratio, including film 5 where the (111) line is absent. Nonetheless we find calculated values of L_{21} for our films range from 0 (film 5) to 0.62 (film 1) (see also Fig. 7) which compare favorably with values calculated by Wang *et al.* [17].

The out-of-plane lattice constants were calculated using the (004) reflection and are also shown in Table I. All films annealed at or above 400°C for 60 min exhibited a lattice constant close to the bulk lattice constant value of 0.5767 nm [44]. As illustrated in Table I, within experimental uncertainties the out-of-plane lattice constant was not observed to be strongly sensitive to changes in the (111)/(004) ratio, i.e., the L_{21} ordering, the exception being film 5, the most disordered film with a significantly larger out-of-plane lattice constant, although we note that the uncertainty was found to be also larger at ± 0.001 . We also determined the in-plane lattice constant, measured with an out-of-plane tilt so that the resultant d spacing has contributions from both in- and out-of-plane lattice spacings, e.g., using (111) and (333) lines, among others. Assuming that there is only one value for the in-plane lattice parameter, we found that the in-plane:out-of-plane ratio did not vary systematically within the series and differed from unity by less than 1% except for the most disordered film (film 5) where the ratio is 0.988. Thus, the estimated tetragonal distortion, within two decimal places, is less than 1%, which is consistent with previous reports on crystalline Co_2MnGa films [12,19].

During the optimization process, it was found that the determining factor of the L_{21} ordering was the vacuum pressure after the one hour pregrowth substrate heat treatment, immediately before the Ar gas was introduced into the chamber for the film sputtering. As illustrated in Table I, films with the highest (111)/(004) ratios had starting pressures of 1.5×10^{-7} mbar, whereas film 5 with no visible (111) line had a starting pressure ten times higher of $\sim 15 \times 10^{-7}$ mbar.

The effect of the changing deposition conditions (determining the level of L_{21} ordering) on the electronic properties is clearly shown in Fig. 3, which illustrates the temperature dependent DC resistivity for several films produced during the optimization process. It is observed that with increasing annealing temperature, the magnitude of the resistivity decreases, while the temperature coefficient of resistance increases from near zero for the unannealed film, behavior expected for a highly disordered metal. For an optimized film (right panel; film 1) with a maximum L_{21} order the resistivity is approximately linear in the temperature range between 300 and ~ 130 K indicating that the scattering is dominated by phonons for this film. Between ~ 25 and 130 K the temperature dependence becomes greater than linear and is often considered as indicating another contributing scattering mechanism such as involving magnons [45,46]. Below ~ 20 K we observe an upturn in the resistivity going as $-T^{1/2}$. The slope of this upturn decreases with increasing annealing temperature which is consistent with suggestions that the $-T^{1/2}$ behavior is due to electron-electron interactions in the presence of disorder or weak localization [47], which are minimized for the highest L_{21} ordered films. We find that for less optimized films (left and middle panels in Fig. 3) the low-temperature upturn is more prominent, and starts at a higher temperature, and the high-temperature linear region is restricted to a smaller, higher-temperature region. As will be discussed below, the 300 K DC conductivity values are also employed in the optical modeling process. At 300 K, the anomalous Hall angle $\theta_H = \frac{\sigma_{xy}}{\sigma_{xx}}$, where $\sigma_{xy} = \rho_{xy}/(\rho_{xy}^2 + \rho_{xx}^2)$ and $\sigma_{xx} = \rho_{xx}/(\rho_{xy}^2 + \rho_{xx}^2)$, was observed, with an increasing (111)/(004) ratio, to rise from 6.35% for an unannealed film to 9.84% for a fully optimized film (maximum L_{21} order), with the latter matching observed large anomalous Hall values of Co_2MnGa with Weyl nodal loops in the electronic structure near the Fermi level [16,19,47]. Other than film 1 these unoptimized films are not discussed further.

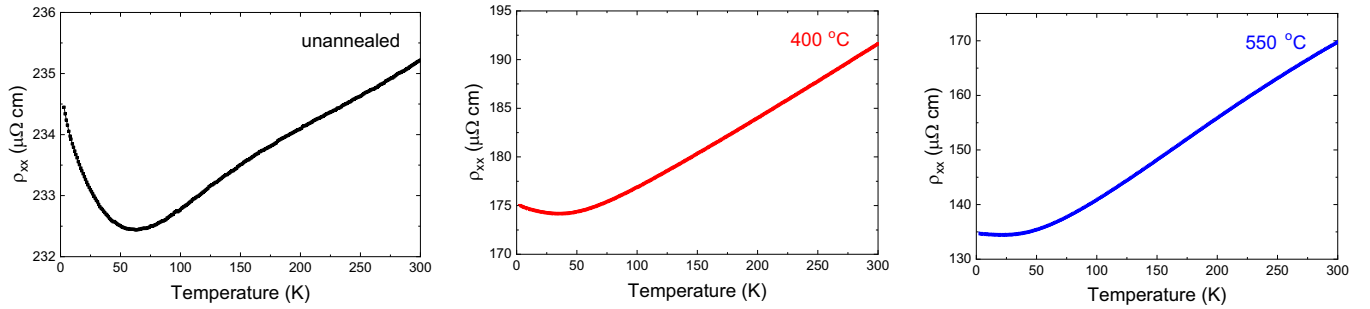


FIG. 3. The longitudinal resistivity for selected Co_2MnGa films all deposited at 400°C followed by annealing for 60 min at different temperatures from unannealed (left panel), 400°C (middle panel), and 550°C (film 1) (right panel). This data set was developed during the optimization process so that only data from film 1 (right panel) are discussed further.

IV. OPTICAL SPECTROSCOPY RESULTS AND DISCUSSION

The optical spectroscopy study was carried out on the selection of films listed in Table I. In Fig. 4(a) we display the measured reflectivity from 10 meV to 6 eV for a 200 nm Co_2MnGa film with the highest (111)/(004) ratio (film 1 in Table I, the film with the largest L_{21} ordering). This film exhibits a metallic-like high reflectivity at low energy falling to small values at 6 eV after passing through a plateau near 1 eV. The film is observed to be nontransparent across the entire spectral range consistent with a low-energy skin depth of 200 nm at 300 K, so the reflectivity only was modeled. For all other films a measurable, although less than 5%, transmission was observed so that the reflectivity and transmission were modeled simultaneously in these films. Figure 4(b) displays the reflectivity and transmission over a spectral range limited to 3.5 eV, for the 100 nm thick film exhibiting no (111) line (film 5, no L_{21} ordering). The reflectivity is significantly reduced although the energy dependent behavior is qualitatively similar. Of note is a strong narrow feature at about 50 meV that we assign to the MgO substrate's optical phonon which, on close inspection, can be seen in both films. The thinner film

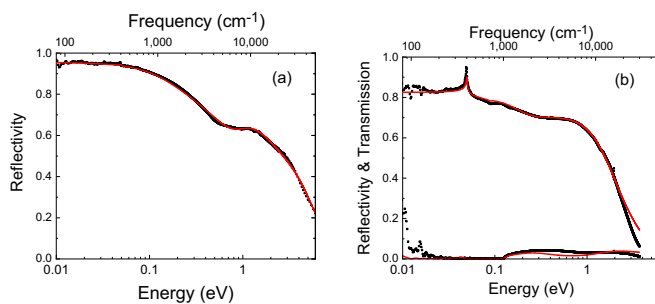


FIG. 4. (a) The measured (black dots) and modeled (red line) reflectivity of a Co_2MnGa 200 nm film with the highest L_{21} order (film 1). (b) The measured (black dots) and modeled (red line) reflectivity and transmission of a Co_2MnGa 100 nm film with no L_{21} order (film 5). For this thinner film there is a measurable transmission rising to about 5% at 0.3 eV which is included in the model. The calculated reflectivity and transmission are based on the dielectric function model discussed in the text. The feature at 50 meV is assigned to phonons in the MgO substrate.

(film 5) has a maximum 5% transmission at energies above the MgO phonon region. Clearly the optical probe samples the whole film.

As reported in our earlier work [34], public domain software package REFFIT [48] was used to model the reflectivity and transmission spectra simultaneously using a Kramers-Kronig consistent sum of Drude-Lorentzian functions to simulate an energy dependent dielectric function, $\varepsilon(\omega) = \varepsilon_1(\omega) + i\varepsilon_2(\omega)$, where

$$\varepsilon(\omega) = \varepsilon_\infty + \sum_k \frac{S_k^2}{\omega_{0k}^2 - \omega^2 - i\gamma_k\omega}.$$

Here ε_∞ is the high-frequency dielectric constant, ω is the frequency, ω_0 is the oscillator frequency, S is the oscillator strength (S is the plasma frequency, $=\omega_p$, for a Drude model at $\omega_0 = 0$) and k denotes the oscillator in question, and γ is the scattering rate when applied to a Drude term or damping when applied to an electronic transition. The REFFIT software package can be applied to multilayered systems, i.e., a thin Heusler alloy film on a thick MgO substrate (0.5 mm). To determine the optical behavior of the film, we first derived an optical model for the MgO substrate by independently measuring its reflectivity and transmission across the full spectral range of interest and using REFFIT to simultaneously model both the reflectivity and transmission to derive a model dielectric function for a single 0.5 mm layer of MgO. Using this model, and the measured reflectivity and transmission of the film/substrate multilayer, the dielectric function of the semitransparent film is then determined. Below we discuss our results in terms of the energy dependent conductivity, which is related to the dielectric function by $\sigma(\omega) = -i\omega\varepsilon(\omega)/4\pi$, which contains information about the response from the free carriers, phonons, and interband transitions to incident light. We use the conductivity as it is an intensive material property which does not depend on the dimensions of a sample; i.e., the conductivity is independent of the film thickness so that the conductivity of all our films can be directly compared [49]. An additional advantage of this approach is that at the zero-energy limit, the optical conductivity can be directly compared with, and is equivalent to, the DC electrical conductivity.

In Fig. 5 we display the absorbing part of the conductivity, $\sigma_1(\omega)$, derived from the model fitted to the data for the two films representing the extreme range of L_{21} order in our

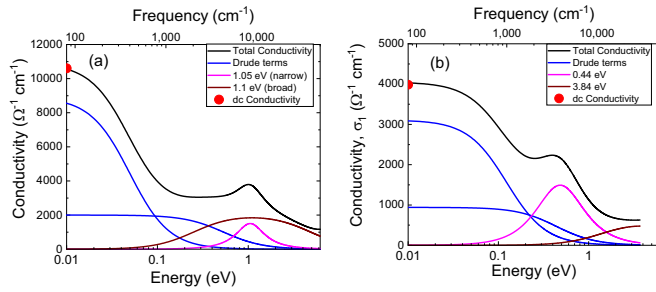


FIG. 5. The real part of the total optical conductivity (black) extracted from the dielectric function fits to the reflectivity spectra in Fig. 4, for (a) film 1 with the highest L_{21} order and (b) film 5 with no L_{21} order. Also shown is the decomposition of the models into two Drude terms (blue) and two Lorentz functions (pink and brown). The DC conductivities are shown by the red points at 0.01 eV, which compare well with the low-energy optical conductivities.

samples, films 1 and 5 shown in Fig. 4. Figure 5 illustrates the separate components of these models, consisting of two Drude terms and two oscillators. The ϵ_∞ term has been accounted for by including an oscillator well above the measured region at about 9 eV. Consistent with the high reflectivity, all films exhibit a strong itinerant-carrier (Drude) response. A constraint we apply to the model is that the low-energy optical conductivity, $\sigma_1(0)$, is consistent with the DC conductivity as determined from electrical transport measurements and is shown as red dots in Fig. 5. The relatively highly conducting nature of all our films shields the Co_2MnGa phonon contribution that is expected around 250 cm^{-1} [50] and so this is not included in the model.

In selecting a two-Drude model, we have been guided by our Co_2MnGa band structure calculation displayed in Fig. 6(a), which is consistent with calculations reported by previous studies [2,3,5,11]. These calculations indicate that Co_2MnGa exhibits nested hole pockets in the minority spin channel centered at Γ and multiple electron/hole pockets in the majority spin channel at the zone boundaries near X , K , and W , suggesting that the best approach would be a multi-band Drude model. Such an approach has been used to model spectra of other semimetals [51,52]. In practice, we find that either a two-band carrier model, or a model composed of a single-band carrier plus an extra oscillator at 0.12 eV, can produce equally good fits to the data.

Of the two Drude terms illustrated in Fig. 5, one term is narrow as it has a significantly lower scattering rate, while the second term is significantly broader. We identify the stronger and narrower Drude term, that contributes most to the low-energy response, as due to majority spin carriers. This is based on the calculation in Fig. 6 which shows a higher density of states for this spin polarization. For film 1, with the largest L_{21} order [Fig. 5(a)], the scattering rate of the narrow Drude term is 0.05 eV ($7 \times 10^{13}\text{ s}^{-1}$). As the L_{21} ordering decreases to zero the scattering rate increases by a factor of nearly 3 to 0.13 eV ($19 \times 10^{13}\text{ s}^{-1}$). These optically determined scattering rates are of a similar magnitude to estimates for other Heusler compounds [29]. The plasma frequency conversely is relatively independent of order, varying by only

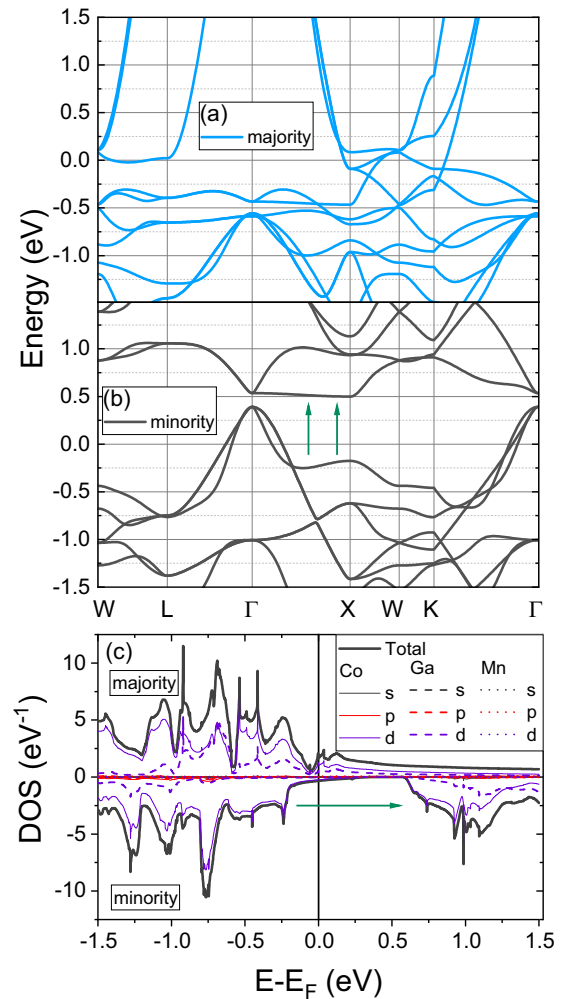


FIG. 6. Calculated band structure of L_{21} ordered Co_2MnGa for (a) the majority spin band, (b) the minority spin band, and (c) the total density of states for each spin polarization. The atom labels apply to both panels in 6(c). Although gapped, note the finite density of states at E_F for the minority spin polarization and the higher density of states at E_F for the majority spin polarization. Arrows in panels (b), (c) indicate the interband transition we argue is the major contributor to the ~ 1 eV peak observed in σ_1 (see Fig. 5).

5% across the range of films studied, which we deem to be within experimental uncertainties. The second, broader Drude term exhibits a significantly higher scattering rate of 0.37 eV ($56 \times 10^{13}\text{ s}^{-1}$) which is independent of the changing order. This result indicates that with changing atomic order, changes in the low-energy optical conductivity are largely driven by a change in the scattering rate rather than the ratio of carrier density (n) to effective mass (m_e), as represented by the plasma frequency ($\omega_p^2 = 4\pi e^2 n/m_e$). This result is broadly consistent with the DC resistivity exhibited in Fig. 3 which tends toward being approximately temperature independent for the film with no L_{21} order (film 5) to exhibiting a significant temperature dependence for the film with the highest L_{21} order (film 1). That is, the closer the structure approaches full L_{21} order, the lower the carrier scattering rate. Band structure calculations for Co_2MnGa indicate that with increasing Co

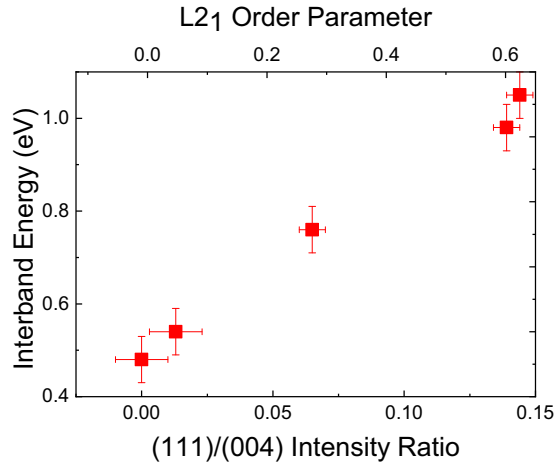


FIG. 7. The energy of the narrow oscillator dominating the interband region in Fig. 4 plotted against the proxy for the L_{21} order parameter, the ratio of the XRD line intensities (111)/(004), for a selection of Co_2MnGa films demonstrating the strong sensitivity of this interband absorption to atomic order. On the upper horizontal axis, we have included the calculated L_{21} order parameter for each film.

antisite and/or Mn/Ga disorder additional states appear within the minority spin gap. This new population creates additional states into which the carriers can scatter, thus allowing for an increased scattering rate as the atomic order decreases. Picozzi *et al.* [53] have noted that these new minority spin states will be localized and, although rapidly screened, would account for the observed threefold increase in the scattering rate exhibited by the itinerant carriers as the density of states in the minority gap grows.

Turning to the interband transitions we note that the two oscillators displayed in Fig. 5 exhibit measurable strength at relatively low energies, i.e., below 0.1 eV. Both these oscillators also shift in energy in ways that depend on the degree of the order although with a quite different dependence. As illustrated in Fig. 7, with increasing L_{21} order, the narrower oscillator that can be seen as a plateau in $R(\omega)$ near 1 eV or a peak in our $\sigma_1(\omega)$ data and the data of Rhee *et al.* [31] moves rapidly to higher energies from ~ 0.5 to ~ 1.0 eV as the L_{21} order increases. The estimated error in the energy position of this oscillator, ± 0.05 eV, is based on the range of parameters producing reasonable fits. The errors in the (111)/(004) ratio increase significantly as the relative noise in the (111) line grows as it becomes smaller. The highly damped oscillator conversely exhibits a large shift to lower energy with increasing disorder, i.e., as the (111)/(004) ratio decreases.

To better understand the origin of the interband transitions we observe in our measurements, we turn to *ab initio* band structure calculations. For the ideal L_{21} structure at zero temperature, these indicate that the band structure near the Fermi energy is dominated by Co-Co-Mn d - d hybridized bands; see, for example, Refs. [2,3,5,11] and the resultant density of states (DOS) plotted in Fig. 6(b). A more direct comparison with the experimentally determined $\sigma_1(\omega)$ can be made by inspecting the joint density of states (jDOS) [54]; however, such

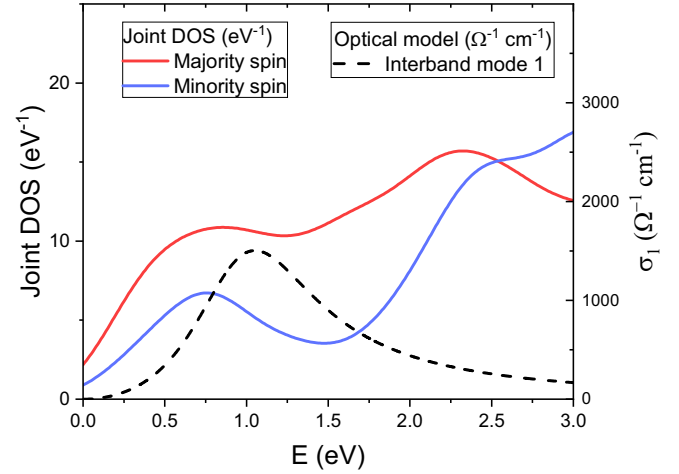


FIG. 8. Comparing the calculated joint density of states (left axis) and experimentally derived $\sigma_1(\omega)$ reproduced from Fig. 5(a) (right axis) for the sample with highest L_{21} order.

a comparison is still qualitative at best and more advanced computational methods are required to attempt quantitative calculation. This quantity is plotted in Fig. 8 for both the minority and majority spin bands. Also shown in the figure is the narrower interband mode determined from experiment and reproduced from Fig. 5(a). We note the structure in the jDOS around 0.7 eV, close in energy to the peak in our optical data, originates from a peak in the minority spin band jDOS, but also with a somewhat featureless contribution from the majority bands. At higher energies, our $\sigma_1(\omega)$ data do not resemble the calculated jDOS.

As illustrated in Fig. 7, the shift to lower energy of the peak in $\sigma_1(\omega)$ follows the loss of L_{21} structure due to the growth of atomic disorder. For a range of Co_2MnZ compositions ($Z = \text{Al, Si, Ge}$), Picozzi *et al.* [53] and Özdoğan and Galanakis [55] have shown that an increase in Co antisite disorder reduces the d -band hybridization, in turn reducing the exchange splitting at the Co antisite, thus reducing the minority spin band gap. These authors also show that this gap is insensitive to Mn/X disorder. These arguments apply only in part to Co_2MnGa where, for the minority spin channel in the ideal structure, the Fermi energy lies in a region of a small but finite density of states near the bottom of the gap. The decreasing atomic order, either Co antisites or atomic swaps, will increase the density of states in the minority spin gap. We then assign the order-sensitive peak in $\sigma_1(\omega)$ (Figs. 5 and 8) to a low-energy minority spin channel interband transition, likely deriving from the transitions between the valence and conduction bands running largely in parallel along the Γ - X direction; see arrow annotations in Fig. 6. This absorption softens quickly with decreasing L_{21} structure due to a reduced d -band hybridization and minority spin gap, resulting from increasing atomic disorder.

V. CONCLUSION

We have undertaken an optical spectroscopic study of epitaxial films of Co_2MnGa to explore near Fermi energy valence

and conduction band intra- and interband transitions. The films are distinguished by their degree of $L2_1$ order, characterized by the ratio of the intensities of the (111) and (004) lines from XRD. Guided by our band structure calculations, we have modeled our spectra with two Drude terms and two Lorentz oscillators, although we find that the data can be fit equally well with either one- or two-band Drude models. A narrow Drude term common to both models indicates that the scattering rate of the itinerant carriers increases threefold with increasing atomic disorder, while the carrier density to effective mass ratio is unchanged. We have assigned the oscillator that dominates the interband spectral region near 1 eV to transitions across the minority spin gap along the Γ -X direction. It is found that the energy of this transition decreases rapidly with increasing disorder consistent with band structure calculations predicting that the size and depth of the minority spin gap in Co_2MnGa is strongly sensitive to atomic ordering.

ACKNOWLEDGMENTS

The authors would like to thank Ted Trewick and the late Martin Ryan for help with the XRD measurements. We also thank Samer Kurdi for helpful advice on determining the structural ordering from XRD measurements. This research was supported by a University Research Fund grant from Victoria University of Wellington. The MacDiarmid Institute for Advanced Materials and Nanotechnology is supported under the New Zealand Centres of Research Excellence Programme. Y.Y. and N.M. gratefully acknowledge computational support from the NCI computational facility and Pawsey Supercomputing Facility. Y.Y. and N.V.M. acknowledge the support from the ARC Centre of Excellence in Future Low-Energy Electronics Technologies (Grant No. CE170100039) and the computational support from Australian National Computing Infrastructure (NCI) and the Pawsey Supercomputing Centre.

- [1] T. Graf, C. Felser, and S. S. P. Parkin, *Prog. Solid State Chem.* **39**, 1 (2011).
- [2] G. Chang, S.-Y. Xu, X. Zhou, S.-M. Huang, B. Singh, B. Wang, I. Belopolski, J. Yin, S. Zhang, A. Bansil, H. Lin, and M. Z. Hasan, *Phys. Rev. Lett.* **119**, 156401 (2017).
- [3] K. Manna, Y. Sun, L. Muechler, J. Kübler, and C. Felser, *Nat. Rev. Mater.* **3**, 244 (2018).
- [4] B. A. Bernevig, C. Felser, and H. Beidenkopf, *Nature (London)* **603**, 41 (2022).
- [5] I. Galanakis, P. H. Dederichs, and N. Papanikolaou, *Phys. Rev. B* **66**, 174429 (2002).
- [6] V. K. Kushwaha, S. Kokado, S. Kasai, Y. Miura, T. Nakatani, R. Kumara, H. Tajiri, T. Furubayashi, K. Hono, and Y. Sakuraba, *Phys. Rev. Mater.* **6**, 064411 (2022).
- [7] S. Skaftouros, K. Ozdogan, E. Sasioglu, and I. Galanakis, *Phys. Rev. B* **87**, 024420 (2013).
- [8] K. Manna, L. Muechler, T.-H. Kao, R. Stinshoff, Y. Zhang, J. Gooth, N. Kumar, G. Kreiner, K. Koepf, R. Car, J. Kübler, G. H. Fecher, C. Shekhar, Y. Sun, and C. Felser, *Phys. Rev. X* **8**, 041045 (2018).
- [9] I. Galanakis, *J. Phys. D: Appl. Phys.* **39**, 765 (2006).
- [10] I. Belopolski, K. Manna, D. S. Sanchez, G. Chang, B. Ernst, J. Yin, S. S. Zhang, T. Cochran, N. Shumiya, H. Zheng, B. Singh, G. Bian, D. Multer, M. Litskevich, X. Zhou, S.-M. Huang, B. Wang, T.-R. Chang, S.-Y. Xu, A. Bansil *et al.*, *Science* **365**, 1278 (2019).
- [11] T. Kono, M. Kakoki, T. Yoshikawa, X. Wang, K. Sumida, T. Muro, K. Goto, Y. Sakuraba, R. Y. Umetsu, and A. Kimura, *Phys. Rev. B* **104**, 195112 (2021).
- [12] A. Markou, D. Krieger, J. Gayles, L. Zhang, Y.-C. Chen, B. Ernst, Y.-H. Lai, W. Schnelle, Y.-H. Chu, Y. Sun, and C. Felser, *Phys. Rev. B* **100**, 054422 (2019).
- [13] A. Sakai, Y. P. Mizuta, A. A. Nugroho, R. Sihombing, T. Koretsune, M.-T. Suzuki, N. Takemori, R. Ishii, D. Nishio-Hamane, R. Arita, P. Goswami, and S. Nakatsuji, *Nat. Phys.* **14**, 1119 (2018).
- [14] J. Hu, Y. Zhang, M. A. Cabero Z., B. Wei, S. Tu, S. Liu, D. Yu, J.-P. Ansermet, S. Granville, and H. Yu, *J. Magn. Magn. Mater.* **500**, 166397 (2020).
- [15] L. Leiva, S. Granville, Y. Zhang, S. Dushenko, E. Shigematsu, T. Shinjo, R. Ohshima, Y. Ando, and M. Shiraishi, *Phys. Rev. B* **103**, L041114 (2021).
- [16] K. Sumida, Y. Sakuraba, K. Masuda, T. Kono, M. Kakoki, K. Goto, W. Zhou, K. Miyamoto, Y. Miura, T. Okuda, and A. Kimura, *Commun. Mater.* **1**, 89 (2020).
- [17] Q. Wang, Z. Wen, T. Kubota, T. Seki, and K. Takanashi, *Appl. Phys. Lett.* **115**, 252401 (2019).
- [18] Y. Sakuraba, K. Hyodo, A. Sakuma, and S. Mitani, *Phys. Rev. B* **101**, 134407 (2020).
- [19] Y. Zhang, Y. Yin, G. Dubuis, T. Butler, N. V. Medhekar, and S. Granville, *npj Quantum Mater.* **6**, 17 (2021).
- [20] C. Guillemard, S. Petit-Watelot, T. Devolder, L. Pasquier, P. Boulet, S. Migot, J. Ghanbaja, F. Bertran, and S. Andrieu, *J. Appl. Phys.* **128**, 241102 (2020).
- [21] P. J. Webster, *J. Phys. Chem. Solids* **32**, 1221 (1971).
- [22] Y. Takamura, R. Nakane, and S. Sugahara, *J. Appl. Phys.* **105**, 07B109 (2009).
- [23] S. Kurdi, Y. Sakuraba, K. Masuda, H. Tajiri, B. Nair, G. F. Nataf, M. E. Vickers, G. Reiss, M. Meinert, S. S. Dhesi, M. Ghidini, and Z. H. Barber, *J. Phys. D: Appl. Phys.* **55**, 185305 (2022).
- [24] M. Jourdan, J. Minár, J. Braun, A. Kronenberg, S. Chadov, B. Balke, A. Gloskovskii, M. Kolbe, H. J. Elmers, G. Schönhense, H. Ebert, C. Felser, and M. Kläui, *Nat. Commun.* **5**, 3974 (2014).
- [25] C. Guillemard, S. Petit-Watelot, L. Pasquier, D. Pierre, J. Ghanbaja, J.-C. Rojas-Sánchez, A. Bataille, J. Rault, P. Le Fèvre, F. Bertran, and S. Andrieu, *Phys. Rev. Appl.* **11**, 064009 (2019).
- [26] R. Mahat, U. Karki, K. C. Shambhu, J. Y. Law, V. Franco, I. Galanakis, A. Gupta, and P. LeClair, *Phys. Rev. Mater.* **6**, 064413 (2022).
- [27] K. Özdoğan, E. Şaşıoğlu, B. Aktaş, and I. Galanakis, *Phys. Rev. B* **74**, 172412 (2006).
- [28] B. Wu, H. Yuan, A. Kuang, Y. Feng, and H. Chen, *J. Phys. D: Appl. Phys.* **44**, 405301 (2011).
- [29] E. I. Shreder, A. A. Makhnev, K. G. Suresh, M. G. Kostenko, E. D. Chernov, V. G. Ivanov, and A. V. Lukoyanov, *Mod. Phys. Lett. B* **36**, 2150573 (2022).

- [30] E. I. Shreder, A. D. Svyazhin, and A. A. Makhnev, *Opt. Spectrosc.* **119**, 969 (2015).
- [31] J. Y. Rhee, Y. V. Kudryavtsev, K. W. Kim, and Y. P. Lee, *ASEAN J. Sci. Technol. Dev.* **24**, 1 (2007).
- [32] A. Bittar, G. V. M. Williams, N. Strickland, C. Grigorescu, O. Monnereau, L. Tortet, M. Autric, E. Valerio, H. J. Trodahl, S. Granville, and B. Ruck, in *Proceedings of the 2006 International Conference on Nanoscience and Nanotechnology* (IEEE, New York, 2006), p. 370.
- [33] K. W. Kim, R. J. Kim, Y. P. Lee, J. Y. Rhee, and Y. V. Kudryavtsev, *J. Korean Phys. Soc.* **49**, 2180 (2006).
- [34] R. G. Buckley, T. Butler, C. Pot, N. M. Strickland, and S. Granville, *Mater. Res. Express* **6**, 106113 (2019).
- [35] M. M. Kirillova, A. A. Makhnev, E. I. Shreder, V. P. Dyakina, and N. B. Gorina, *Phys. Status Solidi* **187**, 231 (1995).
- [36] D. P. Rai, A. S. Sandeep, A. P. Sakhya, T. P. Sinha, R. Khenata, M. P. Ghimire, and R. K. Thapa, *Mater. Res. Express* **3**, 075022 (2016).
- [37] J. T. Armstrong, J. J. Donovan, and P. C. Carpenter, *Microsc. Microanal.* **19**, 812 (2013).
- [38] N. W. M. Ritchie, *Microsc. Microanal.* **15**, 454 (2009).
- [39] K. Momma and F. Izumi, *J Appl. Cryst.* **44**, 1272 (2011).
- [40] H. Ehrenreich, H. R. Philipp, and B. Segall, *Phys. Rev.* **132**, 1918 (1963).
- [41] J. P. Perdew, K. Burke, and M. Ernzerhof, *Phys. Rev. Lett.* **78**, 1396(E) (1997).
- [42] G. Kresse and J. Furthmüller, *Phys. Rev. B* **54**, 11169 (1996).
- [43] Y. Takamura, R. Nakane, and S. Sugahara, *J. Appl. Phys.* **107**, 09B111 (2010).
- [44] K. H. J. Buschow and P. G. van Engen, *J. Magn. Magn. Mater.* **25**, 90 (1981).
- [45] S. Tong, X. Zhao, D. Wei, and J. Zhao, *Phys. Rev. B* **101**, 184434 (2020).
- [46] L. Zhu and J. Zhao, *Sci. Rep.* **7**, 42931 (2017).
- [47] I. Belopolski, G. Chang, T. A. Cochran, Z.-J. Cheng, X. P. Yang, C. Hugelmeier, K. Manna, J.-X. Yin, G. Cheng, D. Multer, M. Litskevich, N. Shumiya, S. S. Zhang, C. Shekhar, N. B. M. Schröter, A. Chikina, C. Polley, B. Thiagarajan, M. Leandersson, J. Adell *et al.*, *Nature (London)* **604**, 647 (2022).
- [48] B. Kuzmenko, *Rev. Sci. Instrum.* **76**, 083108 (2005).
- [49] F. Reif, *Fundamentals of Statistical and Thermal Physics* (McGraw-Hill, New York, 1965).
- [50] A. Candan, G. Uğurb, Z. Charific, H. Baazizc, and M. R. Ellialtıođlu, *J. Alloys Compd.* **560**, 215 (2013).
- [51] Z. Ni, B. Xu, M.-Á. Sánchez-Martínez, Y. Zhang, K. Manna, C. Bernhard, J. W. F. Venderbos, F. de Juan, C. Felser, A. G. Grushin, and L. Wu, *npj Quantum Mater.* **5**, 96 (2020).
- [52] L. Z. Maulana, K. Manna, E. Uykur, C. Felser, M. Dressel, and A. V. Pronin, *Phys. Rev. Res.* **2**, 023018 (2020).
- [53] S. Picozzi, A. Continenza, and A. J. Freeman, *Phys. Rev. B* **69**, 094423 (2004).
- [54] V. Wang, N. Xu, J.-C. Liu, G. Tang, and W.-T. Geng, *Comput. Phys. Commun.* **267**, 108033 (2021).
- [55] K. Özdođan and I. Galanakis, *J. Appl. Phys.* **110**, 076101 (2011).